

Thermal Stability and Phase Transformation of Conductive α -(Al_xGa_{1-x})₂O₃/Ga₂O₃ Heterostructure on Sapphire Substrates

Botong Li^{1,*}, Shisong Luo^{2,*}, Jaeheon Jung^{3,*}, Bobby G. Duersch⁴, Cheng Chang², Lucas Lau², Zonghao Zhang², Jianhua Li⁵, Hunter Ellis¹, Imteaz Rahaman¹, Roy Byung Kyu Chung^{3, a)}, Kai Fu^{1, a)}, and Yuji Zhao^{2, a)}

AFFILIATIONS

¹Department of Electrical and Computer Engineering, University of Utah, Salt Lake City, UT 84112, USA

²Department of Electrical and Computer Engineering, Rice University, Houston, TX 77005, USA

³Advanced Materials Science and Engineering Department, Kyungpook National University, Daegu 41566, Republic of Korea

⁴Utah Nanofab Electron Microscopy and Surface Analysis Laboratory, The University of Utah, Salt Lake City, UT 84112, USA

⁵Shared Equipment Authority, Rice University, Houston, Texas 77005, USA

* Authors contribute equally to this work.

^{a)} Authors to whom correspondence should be addressed: roy.b.chung@knu.ac.kr, kai.fu@utah.edu, and yuji.zhao@rice.edu

Abstract

Thermal stability and phase transformation of conductive α -(Al_{0.16}Ga_{0.84})₂O₃/Ga₂O₃ heterostructure on sapphire substrates were investigated via in situ high temperature X-ray diffraction (HT-XRD), scanning electron microscopy (SEM), and atomic force microscopy (AFM). The conductive α -(Al_{0.16}Ga_{0.84})₂O₃/Ga₂O₃ heterostructure with fluorine (F) doping were growth by mist CVD on sapphire substrates, which achieved a Hall mobility of 28 cm²/(V·s) and electron concentration of 1.4×10²⁰ cm⁻³. The heterostructure exhibited thermal stability to ~550-575°C before transforming to β -(Al_xGa_{1-x})₂O₃/Ga₂O₃. The transformed β -Ga₂O₃ is mainly polycrystalline rather than a high-quality epitaxial phase. Reciprocal space mapping (RSM) results reveal that the edge dislocation density remains consistently higher than the screw dislocation density throughout the entire heating process, indicating that the crystalline imperfection in α -Ga₂O₃ is dominated by in-plane mosaicism. After the phase transformation of α phase to β phase, catastrophic damage to the film and upheaval of the surface were observed by SEM and AFM.

Keywords

α -(Al_xGa_{1-x})₂O₃/Ga₂O₃, XRD, high temperature, phase transformation, thermal stability

Ga₂O₃ has attracted significant interest in power electronics ¹, solar-blind detectors ², and high temperature electronics ³ due to its ultrawide bandgap and high breakdown electrical field. Ga₂O₃ is polymorphic, with the orthorhombic-

structured Ga_2O_3 (β - Ga_2O_3) being the thermodynamically stable form⁴. With the largest bandgap of ~ 5.3 eV^{5,6} among all the polymorphs, corundum-structured Ga_2O_3 (α - Ga_2O_3) is a promising alternative material for applications in high-power electronics, as indicated by its higher Baliga figure of merit (BFOM) than β -phase Ga_2O_3 ⁷. α - Ga_2O_3 could be grown on isomorphic sapphire (α - Al_2O_3), of which large-scale wafers are commercialized at a reasonable price. Currently, conductivity control of n-type doping (mainly achieved by Sn or Si dope) α - Ga_2O_3 could be grown by mist-chemical vapor deposition (mist-CVD)^{8,9}, pulsed laser deposition (PLD)¹⁰, halide vapor phase epitaxy (HVPE)¹¹, and suboxide molecular-beam epitaxy (S-MBE)¹².

Moreover, α - Ga_2O_3 is able to form alloys with other corundum-structured oxides, such as III-oxides α - Al_2O_3 and α - In_2O_3 , offering a bandgap energy tunable in wide range of 3.7-8.6 eV^{13,14}. Specifically, α -($\text{Al}_x\text{Ga}_{1-x}$)₂ O_3 can be grown without a compositional limitation¹⁵ compared to β -($\text{Al}_x\text{Ga}_{1-x}$)₂ O_3 . ($\text{Al}_x\text{Ga}_{1-x}$)₂ O_3 covers 5.3-8.6 eV bandgap range and is predicted to exhibit one of the highest theoretical BFOM among ultra-wide-bandgap semiconductors. Currently, α -($\text{Al}_x\text{Ga}_{1-x}$)₂ O_3 has been introduced as a buffer layer in α - Ga_2O_3 -on-sapphire based devices to reduce the lattice mismatch between α - Ga_2O_3 and sapphire substrate, which could improve α - Ga_2O_3 crystalline quality and hence device performance¹⁶. For example, benefited from the improved epitaxial quality with an α -($\text{Al}_{0.24}\text{Ga}_{0.76}$)₂ O_3 intermediate layer, a smaller dark current and a higher responsivity are achieved in α - Ga_2O_3 based solar-blind detectors¹⁷. Similarly, due to the improved crystalline quality using the graded α -($\text{Al}_x\text{Ga}_{1-x}$)₂ O_3 layer, a larger breakdown voltages and forward current density are obtained in an α - Ga_2O_3 Schottky diodes¹⁸. Moreover, band-offset engineering in α -($\text{Al}_x\text{Ga}_{1-x}$)₂ O_3 / Ga_2O_3 and progress in donor doping and heterostructure growth provide the materials basis for high electron mobility transistors (HEMT) to further improve Ga_2O_3 devices' performance¹⁹⁻²³. Although modulation-doped α -phase HEMT remains less established in the open literature, modulation-doped β -($\text{Al}_x\text{Ga}_{1-x}$)₂ O_3 / Ga_2O_3 heterostructures for HEMT have been demonstrated^{24,25}. Therefore, more effort is required to investigate the properties of α -($\text{Al}_x\text{Ga}_{1-x}$)₂ O_3 / Ga_2O_3 heterostructures.

As metastable phase, one challenge of α -($\text{Al}_x\text{Ga}_{1-x}$)₂ O_3 / Ga_2O_3 heterostructures is its thermal stability. Moreover, first principles calculations find that the thermal conductivity of α - Ga_2O_3 is low (8.0-11.6 W/mK)²⁶. High temperatures environments occur during device fabrication processes and applications. Ion implantation is attractive for Ga_2O_3 device since it provides conductivity control in the lateral directions²⁷. Implanted dopants require high temperature annealing to activate the carrier. Specifically, anneal temperature up to 900-1000 °C is required in β - Ga_2O_3 with Si-ion implantation doping²⁸. Other processes such as ohmic contact also involve high temperature anneals^{29,30}. Besides, under a high-power and high-frequency operation, Ga_2O_3 based electronics faced an extremely high-power density and high-power loss. They lead to a high channel temperature that could be higher than 180 °C characterized by micro-Raman in a α - Ga_2O_3 MOSFET³¹ and higher than 330 °C characterized by infrared thermal imaging in a β - Ga_2O_3 MOSFET³².

The thermal stability of α - Ga_2O_3 and α -($\text{Al}_x\text{Ga}_{1-x}$)₂ O_3 have been studied both in theory³³ and experiment³⁴⁻³⁹. The growth method includes mist-CVD^{34,35,37}, ALD³⁶, MBE³⁸, and HVPE³⁹. Previous study observed that the phase transformation temperature of α - Ga_2O_3 is dependent to thickness of α - Ga_2O_3 ³⁷ and that of α -($\text{Al}_x\text{Ga}_{1-x}$)₂ O_3 is dependent to Al concentration³⁵. However, no studies have investigated the thermal stability and phase transformation

of the $\alpha\text{-}(\text{Al}_x\text{Ga}_{1-x})_2\text{O}_3/\text{Ga}_2\text{O}_3$ heterostructures. Moreover, most works do not focus on conductive $\alpha\text{-}\text{Ga}_2\text{O}_3$ or $\alpha\text{-}(\text{Al}_x\text{Ga}_{1-x})_2\text{O}_3$ thin films, which are essential for application in power electronics.

This Letter reports the investigations of the thermal stability and phase transformation of conductive $\alpha\text{-}(\text{Al}_x\text{Ga}_{1-x})_2\text{O}_3/\text{Ga}_2\text{O}_3$ heterostructure on c-plane sapphire ((0001)) substrates using *in situ* high temperature X-ray diffraction (HT-XRD) up to 1000°C, including $2\theta\text{-}\omega$ scan, rocking-curve (RC), and reciprocal space mapping (RSM). As shown in Figure 1(a), 1-μm-thick $\alpha\text{-}\text{Ga}_2\text{O}_3$ film followed by 100 nm $\alpha\text{-}(\text{Al}_x\text{Ga}_{1-x})_2\text{O}_3$ was grown on sapphire by mist-CVD⁴⁰. For $\alpha\text{-}\text{Ga}_2\text{O}_3$, gallium acetylacetone ($\text{Ga}(\text{acac})_3$) was dissolved in deionized water (DI water) with a small amount of HCl to prepare the solution. The solution was atomized using a 1.7 MHz transducer, and the mist was carried into a CVD reactor at 450 °C by N_2 carrier gas. Under these conditions, the growth rate was approximately 17 nm/min, and an $\alpha\text{-}\text{Ga}_2\text{O}_3$ layer with a thickness of ~1 μm was obtained after 60 min. For $\alpha\text{-}(\text{Al}_x\text{Ga}_{1-x})_2\text{O}_3$, aluminum acetylacetone ($\text{Al}(\text{acac})_3$) and NH_4F were added in deionized water (DI water) with a small amount of HCl to prepare the solution for Al source and F dopant, respectively. Except from the n-type doping, F dopant element also provide better thermal stability in both electrical and structural properties in $\alpha\text{-}\text{Ga}_2\text{O}_3$ than undoped or Sn-doped $\alpha\text{-}\text{Ga}_2\text{O}_3$ as reported in our previous publication⁴⁰. The solution was atomized using the same transducer, and the mist was carried into a CVD reactor at 470 °C by O_2 carrier gas. According to the XRD shown in Figure 1(b) and Bragg's law

$$2ds\sin\theta=n\lambda \quad (1)$$

where $\lambda = 1.5405 \text{ \AA}$ for Cu $\text{K}\alpha_1$ radiation, $n = 6$ for (0006) XRD peak. The lattices constant of c-axis of $\alpha\text{-}\text{Ga}_2\text{O}_3$, $\alpha\text{-}(\text{Al}_x\text{Ga}_{1-x})_2\text{O}_3$, and $\alpha\text{-}\text{Al}_2\text{O}_3$ (sapphire substrate) can be extracted as 13.32 Å, 13.25 Å, and 12.90 Å, respectively. Furthermore, according to Vegard's law of $d_{(\text{Al}_x\text{Ga}_{1-x})_2\text{O}_3} = xd_{\text{Al}_2\text{O}_3} + (1-x)d_{\text{Ga}_2\text{O}_3}$, which has been verified by experiment^{41, 42}, the Al concentration could be expressed as:

$$x = \frac{d_{\text{Ga}_2\text{O}_3} - d_{(\text{Al}_x\text{Ga}_{1-x})_2\text{O}_3}}{d_{\text{Al}_2\text{O}_3} - d_{(\text{Al}_x\text{Ga}_{1-x})_2\text{O}_3}} \quad (2)$$

Even though the lattice constant can be affected by the strain from the substrate, through inserting the extracted lattices constant, the Al composition could be approximately calculated at around $x \approx 0.16$. Electrical properties (including mobility and carrier concentration) of the films were also characterized by Hall measurements (Lakeshore Fast Hall) at room temperature by using the van der Pauw method. Indium was applied for Hall measurements and then removed before XRD measurement. As shown in Figure 1(c), a relatively high mobility and carrier concentration has been achieved compared to other reports, which are $28 \text{ cm}^2/(\text{V}\cdot\text{s})$ and $1.4 \times 10^{20} \text{ cm}^{-3}$, respectively.

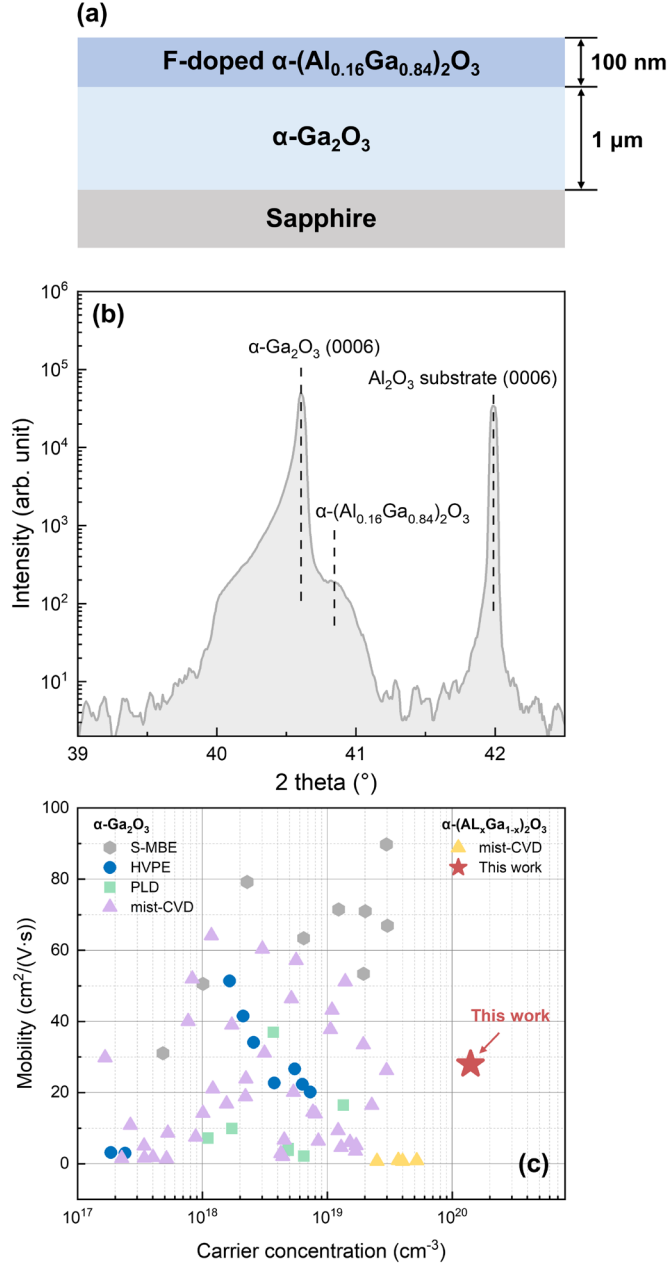


FIG. 1 (a) Schematic of α -(Al_xGa_{1-x})₂O₃/Ga₂O₃ heterostructures on sapphire substrate. (b) XRD 2θ - ω scans at room temperature. (c) Comparison of mobilities of the doped α -Ga₂O₃ or α -(Al_xGa_{1-x})₂O₃ grown by S-MBE ¹², HVPE ¹¹, PLD ¹⁰, and mist-CVD ^{8, 9, 43, 44}, as a function of mobile carrier concentration.

In-situ high-temperature X-ray diffraction (HT-XRD) measurements were performed using a Bruker D8 Discover diffractometer equipped with an Eiger 2R 250k detector and an Anton Paar DHS 1100 heating stage. During heating, the sample was enclosed by a graphite dome to protect the instrument from thermal radiation and to improve temperature uniformity. To evaluate the thermal stability and possible phase transformation of the α -(Al_{0.16}Ga_{0.84})₂O₃/Ga₂O₃ heterostructure, HT-XRD 2 θ - ω scans, rocking curve (RC) scans, and reciprocal space mapping (RSM) were carried out in air atmosphere from 25 °C to 1000 °C, followed by a final scan after cooling back to 25 °C. A finer temperature step was applied between 500 °C and 600 °C to better capture potential onset of phase transformation. The temperature ramp rate between setpoints was 300 °C min⁻¹ up to 500 °C and reduced to 10 °C min⁻¹ above 500 °C. At each set temperature, the sample was held for more than 40 min in total, including the stabilization delay and acquisition time for the 2 θ - ω , RC, and RSM measurements. After the 1000 °C measurement, the sample was cooled from 1000 °C to ~27 °C while maintaining the graphite dome in place, with a cooling duration of approximately 20 min.

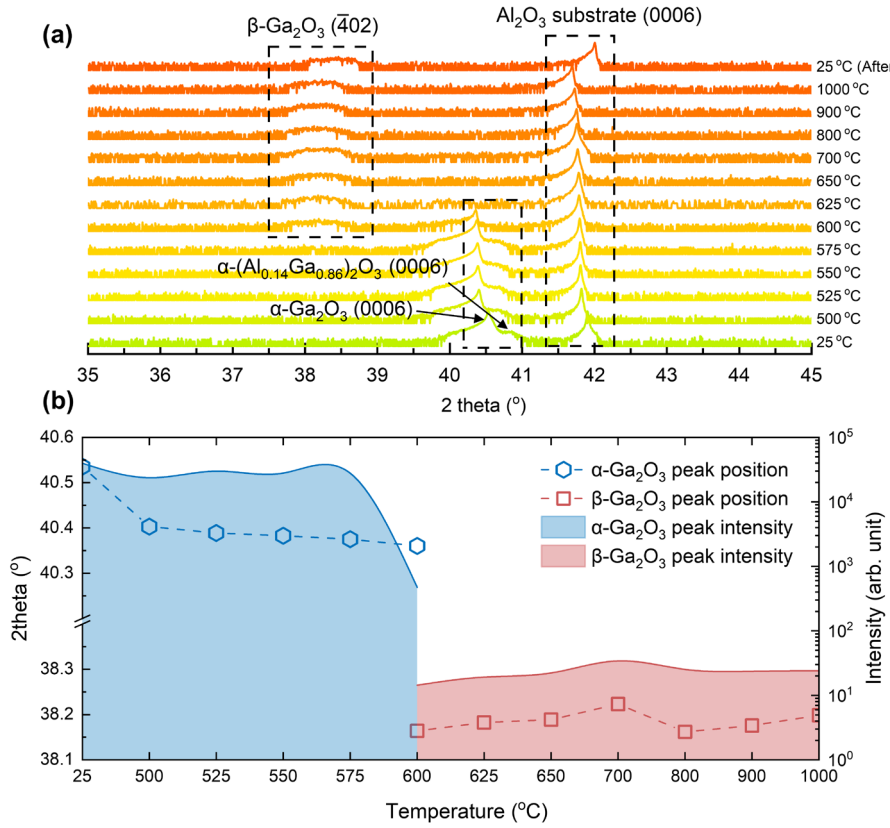


FIG. 2. (a) Temperature-dependent 2 θ - ω XRD scans of the α -(Al_{0.16}Ga_{0.84})₂O₃/Ga₂O₃ sample measured from room temperature to 1000 °C. (b) Extracted peak positions and intensities of the α -Ga₂O₃ and β -Ga₂O₃ diffraction peaks as a function of temperature.

Figure 2(a) shows the temperature-dependent 2 θ - ω XRD scans of the α -(Al_{0.16}Ga_{0.84})₂O₃/Ga₂O₃ heterostructure measured from 25 °C to 1000 °C. At room temperature (25 °C), two dominant diffraction peaks located at approximately 40.5° and 41.6° can be observed, corresponding to the α -Ga₂O₃ (0006) reflection and the sapphire

substrate peak, respectively. As discussed above, a weaker peak appears on the high-angle side of the α -Ga₂O₃ (0006) peak, which is assigned to the α -(Al_{0.16}Ga_{0.84})₂O₃ layer. With increasing temperature, both the α -Ga₂O₃ (0006) peak and the sapphire peak exhibit a continuous shift toward lower 2θ angles, indicating lattice expansion caused by thermal expansion. Notably, when the temperature reaches approximately 575 °C, a weak feature emerges near 38.2°, which is close to the expected position of the β -Ga₂O₃ ($\bar{2}01$) reflection. Upon further heating to 600 °C, the β -Ga₂O₃ ($\bar{2}01$) peak becomes significantly pronounced while the intensity of the α -Ga₂O₃ (0006) peak decreases, suggesting that the α to β phase transformation initiates. When the temperature increases to 625 °C, the α -Ga₂O₃ (0006) peak nearly disappears, and the diffraction pattern is dominated by the substrate peak and a broad β -Ga₂O₃ feature which indicates that the transformed β phase is mainly polycrystalline rather than epitaxially aligned. Further heating up to 1000 °C does not introduce additional phase changes, and the film remains in the β -Ga₂O₃ phase after cooling, consistent with the higher thermodynamic stability of β -Ga₂O₃.

Figure 2(b) summarizes the evolution of the peak position and peak intensity extracted from the temperature-dependent 2θ - ω scans, including the α -Ga₂O₃ (0006) and β -Ga₂O₃ ($\bar{2}01$) reflections. Before 600 °C, the α -Ga₂O₃ (0006) peak remains the dominant film diffraction feature, and its 2θ position continuously shifts toward lower angles with increasing temperature, consistent with lattice thermal expansion. In this temperature range, the α -Ga₂O₃ peak intensity does not show a strong monotonic decrease, indicating that the epitaxial α -phase remains largely preserved prior to the phase transformation. When the temperature reaches approximately 600 °C, a pronounced reduction in the α -Ga₂O₃ (0006) intensity is observed, accompanied by the emergence and rapid growth of the β -Ga₂O₃ ($\bar{2}01$) peak, suggesting the onset of the α to β phase transformation. After the transformation, the β -Ga₂O₃ ($\bar{2}01$) peak becomes the main Ga₂O₃-related reflection aside from the sapphire substrate peak. However, its intensity remains significantly lower, and the diffraction peak is broadened, implying that the transformed β -Ga₂O₃ is mainly polycrystalline rather than a high-quality epitaxial phase. In an ideal single-crystalline material, the coherent Bragg intensity is expected to decrease with increasing temperature due to enhanced atomic thermal vibration, which can be described by the Debye-Waller factor through the temperature-dependent scattering factor as⁴⁵:

$$f = f_0 e^{-M} \quad (3)$$

Here, M increases with temperature and can be expressed as

$$M = 8\pi^2 \bar{u}^2 (\sin\theta/\lambda)^2 \quad (4)$$

where \bar{u}^2 represents the mean-square atomic displacement. Therefore, the diffracted intensity is expected to decrease as temperature increases. In contrast, the β -Ga₂O₃ ($\bar{2}01$) peak shows an overall intensity increase after it first emerges during heating. This means that the β -Ga₂O₃ signal evolves dynamically during the HT-XRD process, consistent with progressive nucleation and grain growth of β -Ga₂O₃. As the temperature increased, the volume fraction of β -Ga₂O₃ increases continuously, resulting in a net gain in the diffracted intensity of the β reflection despite the Debye-Waller attenuation. Meanwhile, the β -Ga₂O₃ peak remains relatively broad compared with the original epitaxial α -Ga₂O₃ peak, suggesting that the transformed β -Ga₂O₃ is primarily polycrystalline with a distribution of grain orientations and/or residual strain. Furthermore, the apparent shift of the β -Ga₂O₃ peak position does not necessarily reflect pure thermal

expansion behavior, because the measured feature likely includes contributions from multiple β -phase grains, overlaps with a broad background, and continuous redistribution of intensity within the broad peak envelope. Therefore, the intensity increases and peak evolution of the β -Ga₂O₃ reflection strongly supports an ongoing structural reconstruction and crystallization process during heating up to 1000 °C.

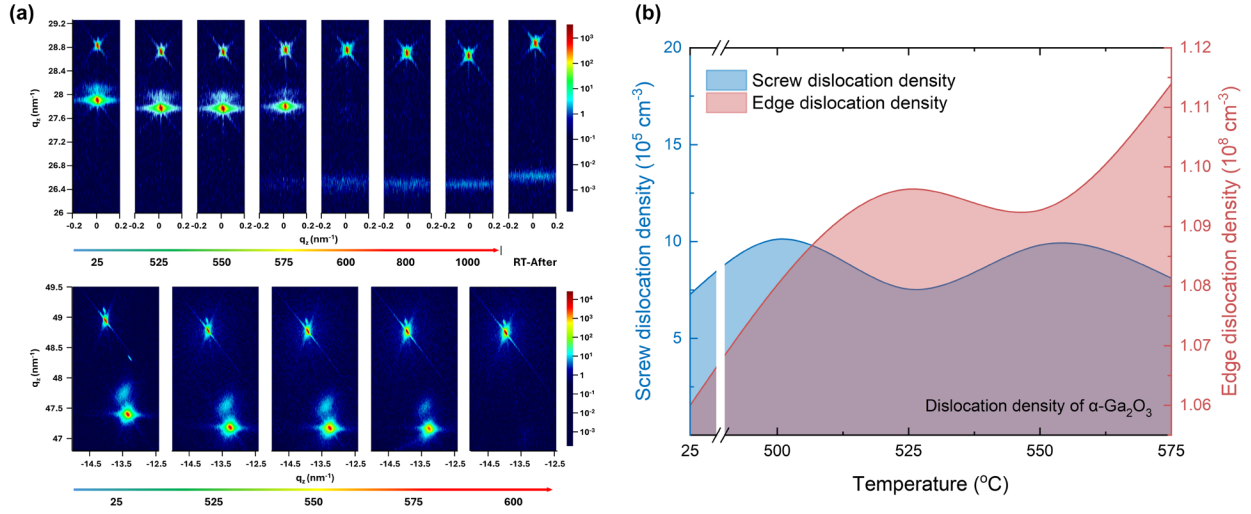


FIG. 3. (a) Temperature-dependent symmetric and asymmetric RSMs of the α -(Al_{0.16}Ga_{0.84})₂O₃/Ga₂O₃ heterostructure measured at selected temperatures during heating. (b) Extracted screw and edge dislocation densities of the α -Ga₂O₃ layer as a function of temperature.

To further resolve the structural evolution during heating and to provide a clearer identification of the phase transformation observed in the 2θ - ω scans, symmetric and asymmetric RSMs were performed at selected temperatures, as shown in Figure 3(a). At 25 °C, the symmetric RSM exhibits three diffraction features distributed from high to low q_z , corresponding to the Al₂O₃ substrate, the α -(Al_{0.16}Ga_{0.84})₂O₃ layer, and the α -Ga₂O₃ layer, respectively. The α -(Al_{0.16}Ga_{0.84})₂O₃ peak is noticeably weaker than the substrate and α -Ga₂O₃ peaks, which can be attributed to its relatively small thickness and/or lower crystalline quality. With increasing temperature, no obvious degradation of the α -(Al_{0.16}Ga_{0.84})₂O₃/Ga₂O₃ diffraction peaks is observed prior to ~575 °C, implying that the α -phase maintains stable crystallinity during heating below the phase-transition temperature. When the temperature reaches 575 °C, a faint diffraction feature emerges at the bottom of the symmetric map along with the intensity degrading of α -(Al_{0.16}Ga_{0.84})₂O₃/Ga₂O₃ peaks, which can be assigned to the phase transition from α -phase to β -Ga₂O₃ ($\bar{2}01$). Upon further heating to 600 °C, the β -Ga₂O₃ ($\bar{2}01$) peak becomes substantially more pronounced, while the α -Ga₂O₃ peak becomes barely observable, suggesting that the α to β phase transformation becomes dominant in this temperature range. A consistent transformation behavior is also observed in the asymmetric RSMs, where the Al₂O₃, α -(Al_{0.16}Ga_{0.84})₂O₃, and α -Ga₂O₃ diffraction peaks at (0 $\bar{1}$ 10) are similarly distributed from top to bottom at low temperature. As the temperature increases, both α -phase peaks progressively lose intensity and become less

distinguishable, further confirming that the α -phase structure becomes unstable during heating. Overall, the temperature-dependent RSM results provide direct reciprocal-space evidence that the α -phase heterostructure begins to transform at approximately 575 °C, and the diffraction response becomes dominated by the newly formed β -Ga₂O₃ phase at 600 °C.

Because an RSM records diffraction intensity as a function of both ω and 2θ , RCs can be extracted at each temperature, enabling evaluation of the corresponding full width at half maximum (FWHM). However, at elevated temperatures, the RC broadening reflects a combination of effects, including thermal vibrations, strain fluctuations, and potentially temperature-induced defect evolution. Despite these contributions, the α -Ga₂O₃ epilayer exhibits a more pronounced FWHM broadening than the substrate, indicating an enhanced contribution from film-specific structural disorder during heating. Therefore, the dislocation density was estimated from the measured FWHM values to quantitatively assess the evolution of crystalline disorder. Figure 3(b) shows the temperature dependence of the screw and edge dislocation densities in the α -Ga₂O₃ epilayer, calculated using the FWHM extracted from the symmetric RC and the asymmetric scan, respectively. The dislocation densities were estimated using the widely adopted relationship⁴⁶:

$$\rho = \frac{\beta^2}{4.35 b^2} \quad (5)$$

where ρ is the dislocation density, β is the FWHM, and b is the magnitude of the relevant Burgers vector, which is approximate c lattice constant and a lattice constant of α -Ga₂O₃ for screw and edge dislocation density, respectively. As shown in Figure 3(b), the edge dislocation density remains consistently higher than the screw dislocation density throughout the entire heating process, indicating that the crystalline imperfection in α -Ga₂O₃ is dominated by in-plane mosaicism. This behavior is expected for heteroepitaxial α -Ga₂O₃ grown on sapphire, where lattice mismatch and thermal stress can preferentially introduce edge-type threading dislocations. Notably, the edge dislocation density shows a continuous increasing trend with increasing temperature, instead of remaining constant. This gradual increase suggests that the α -Ga₂O₃ layer undergoes progressive strain accumulation and defect evolution during high-temperature heating. In addition to intrinsic thermal vibration effects, the high-temperature environment may promote dislocation motion, defect multiplication, and strain relaxation, which can increase the mosaic twist and broaden the asymmetric diffraction response, leading to a higher extracted edge dislocation density. Furthermore, near the onset of the α to β phase transformation (around 575–600 °C), the structural instability associated with phase reconstruction can introduce additional lattice distortion and local strain fields, which further accelerates the degradation of crystalline coherence and contributes to the increased edge dislocation density. In contrast, the screw dislocation density shows a much weaker variation during heating, implying that the out-of-plane tilt component is less sensitive to thermal loading compared with the in-plane distortion.

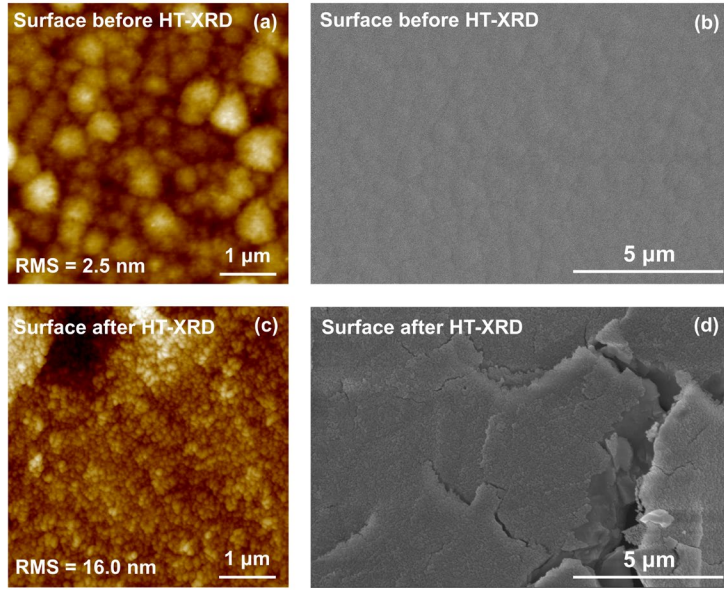


FIG. 4. Surface morphology of the sample before and after high-temperature XRD (HT-XRD). (a) AFM image of the as-grown surface with RMS roughness of 2.5 nm. (b) SEM image of the as-grown sample. (c) AFM image after HT-XRD heating. (d) SEM image after HT-XRD heating.

Figure 4 compares the surface morphology of the sample before and after the HT-XRD heating process using atomic force microscope (AFM) and scanning electron microscope (SEM). As shown in the AFM images in Figures 4(a) and 4(c), the as-grown surface exhibits a relatively uniform granular morphology with a low root-mean-square (RMS) roughness of ~ 2.5 nm, indicating a smooth and continuous film surface prior to heating. After the HT-XRD measurement, the surface becomes significantly roughened, with the RMS roughness increasing to ~ 16.0 nm. Consistent with the AFM results, the SEM images in Figures 4(b) and 4(d) show that the surface changes from a relatively smooth morphology before heating to a much rougher and discontinuous surface after heating. The post-heating SEM image also reveals the formation of large cracks and surface segmentation, indicating mechanical failure induced by thermal processing. This cracking behavior is likely associated with the combined effects of thermal stress, phase transformation, and microstructural reconstruction during the α to β transformation. In particular, the transformation from the epitaxial α -phase to the β - Ga_2O_3 phase is accompanied by a loss of coherent epitaxial registry and the formation of polycrystalline domains, which introduces localized strain and stress concentration, thereby promoting crack initiation and propagation. Therefore, the strong roughening and cracking observed after heating provide direct morphological evidence supporting the diffraction results that the film undergoes significant structural degradation and becomes dominated by a non-epitaxial β - Ga_2O_3 phase after high-temperature annealing.

In summary, thermal stability and phase transformation of conductive α -($\text{Al}_{0.16}\text{Ga}_{0.84}\text{)}_2\text{O}_3/\text{Ga}_2\text{O}_3$ heterostructure on sapphire substrates were investigated via in situ HT-XRD and microscopy investigation. The heterostructure exhibited thermal stability to ~ 550 - 575°C before transforming to β -phase. The resulting β - Ga_2O_3 phase exhibited a broadened diffraction response, indicating that the transformed film is predominantly polycrystalline rather than a high-quality

epitaxial layer. Reciprocal space mapping (RSM) further suggests that the crystalline imperfection in the α -Ga₂O₃ layer is dominated by in-plane mosaicity. After the phase transformation of α phase to β phase, catastrophic damage to the film and upheaval of the surface were observed by SEM and AFM. These results are an important reference for thermal stability of α -(Al_xGa_{1-x})₂O₃/Ga₂O₃-based device.

Acknowledgement

Botong Li, Bobby G. Duersch, Hunter Ellis, Imteaz Rahaman, and Kai Fu acknowledge the support from the University of Utah start-up fund and Research Incentive Seed Grant by the Price College of Engineering and the Vice President for Research (VPR) Office. This work made use of the Nanofab EMSAL shared facilities of the Micron Technology Foundation Inc. Microscopy Suite, sponsored by the John and Marcia Price College of Engineering, Health Sciences Center, Office of the Vice President for Research. In addition, it utilized the University of Utah Nanofab shared facilities, which are supported in part by the MRSEC Program of the NSF under Award No. DMR-112125. Acquisition of the Bruker D8 Discover system was made possible by the Air Force Office of Scientific Research under project number FA9550-21-1-0293. Shisong Luo, Lucas Lau, Cheng Chang, Zonghao Zhang, and Yuji Zhao are supported, in part, by the Nano & Material Technology Development Program through the National Research Foundation of Korea (NRF) funded by the Ministry of Science and ICT (RS-2024-00451173) and, in part, by CHIMES, one of the seven centers in *JUMP 2.0*, a Semiconductor Research Corporation Program by DARPA. The authors would like to acknowledge the use of XRD and AFM of Shared Equipment Authority at Rice University.

Reference

1. M. Xu, A. Biswas, T. Li, Z. He, S. Luo, Z. Mei, J. Zhou, C. Chang, A. B. Puthirath, R. Vajtai, P. M. Ajayan and Y. Zhao, *Applied Physics Letters* **123** (23) (2023).
2. M. Chen, Z. Zhang, B. Wen, J. Kong, R. Zhan, M. Zhao, S. Deng, N. Xu, K. Wang and J. Chen, *Journal of Alloys and Compounds* **1038** (2025).
3. K. Fu, S. S. Luo, H. Q. Fu, K. Hatch, S. R. Alugubelli, H. X. Liu, T. Li, M. F. Xu, Z. B. Mei, Z. Y. He, J. A. Zhou, C. Chang, F. A. Ponce, R. Nemanich and Y. J. Zhao, *Ieee Transactions on Electron Devices* **71** (3), 1641-1645 (2024).
4. S. J. Pearton, J. Yang, P. H. Cary, F. Ren, J. Kim, M. J. Tadjer and M. A. Mastro, *Applied Physics Reviews* **5** (1) (2018).
5. A. Segura, L. Artús, R. Cuscó, R. Goldhahn and M. Feneberg, *Physical Review Materials* **1** (2) (2017).
6. D. Shinohara and S. Fujita, *Japanese Journal of Applied Physics* **47** (9R) (2008).
7. Y. Oshima and E. Ahmadi, *Applied Physics Letters* **121** (26) (2022).
8. K. Akaiwa, K. Kaneko, K. Ichino and S. Fujita, *Japanese Journal of Applied Physics* **55** (12) (2016).
9. K. Akaiwa, K. Ota, T. Sekiyama, T. Abe, T. Shinohe and K. Ichino, *physica status solidi (a)* **217** (3) (2020).

10. S. Vogt, C. Petersen, M. Kneiß, D. Splith, T. Schultz, H. von Wenckstern, N. Koch and M. Grundmann, *physica status solidi (a)* **220** (3) (2023).
11. H. Son, Y.-j. Choi, J.-H. Park, B. Ryu and D.-W. Jeon, *ECS Journal of Solid State Science and Technology* **9** (5) (2020).
12. J. Steele, J. Chen, T. Burrell, N. A. Pieczulewski, D. Bhattacharya, K. Smith, K. Gann, M. O. Thompson, H. G. Xing, D. Jena, D. A. Muller, M. D. Williams, M. K. I. Senevirathna and D. G. Schlom, *APL Materials* **13** (10) (2025).
13. S. Fujita and K. Kaneko, *Journal of Crystal Growth* **401**, 588-592 (2014).
14. S. Fujita, M. Oda, K. Kaneko and T. Hitora, *Japanese Journal of Applied Physics* **55** (12) (2016).
15. R. Jinno, C. S. Chang, T. Onuma, Y. Cho, S. T. Ho, D. Rowe, M. C. Cao, K. Lee, V. Protasenko, D. G. Schlom, D. A. Muller, H. G. Xing and D. Jena, *Sci Adv* **7** (2) (2021).
16. R. Jinno, T. Uchida, K. Kaneko and S. Fujita, *physica status solidi (b)* **255** (4) (2018).
17. X. Sun, Z. Wang, H. Gong, X. Chen, Y. Zhang, Z. Wang, X. Yu, F. Ren, H. Lu, S. Gu, Y. Zheng, R. Zhang and J. Ye, *IEEE Electron Device Letters* **43** (4), 541-544 (2022).
18. B. Kim, D. Yang, W. Sohn, S. Lee, H.-H.-C. Choi, T. Jang, E. Yoon, Y. Park and H. W. Jang, *Acta Materialia* **221** (2021).
19. T. Wang, W. Li, C. Ni and A. Janotti, *Physical Review Applied* **10** (1) (2018).
20. T. Uchida, R. Jinno, S. Takemoto, K. Kaneko and S. Fujita, *Japanese Journal of Applied Physics* **57** (4) (2018).
21. G. T. Dang, S. Sato, Y. Tagashira, T. Yasuoka, L. Liu and T. Kawaharamura, *APL Materials* **8** (10) (2020).
22. A. F. M. A. U. Bhuiyan, Z. Feng, H.-L. Huang, L. Meng, J. Hwang and H. Zhao, *APL Materials* **9** (10) (2021).
23. S. Bin Anooz, T.-S. Chou, A. Akhtar, J. Rehm, H.-H. Chen, Z. Galazka, M. Schmidbauer, M. Albrecht, A. Fiedler and A. Popp, *Journal of Physics D: Applied Physics* **59** (1) (2025).
24. Y. Zhang, A. Neal, Z. Xia, C. Joishi, J. M. Johnson, Y. Zheng, S. Bajaj, M. Brenner, D. Dorsey, K. Chabak, G. Jessen, J. Hwang, S. Mou, J. P. Heremans and S. Rajan, *Applied Physics Letters* **112** (17) (2018).
25. A. Vaidya, C. N. Saha and U. Singisetti, *IEEE Electron Device Letters* **42** (10), 1444-1447 (2021).

26. G. Yang, P. R. Romeo, A. Apostoluk and B. Vilquin, *Journal of Vacuum Science & Technology A* **40** (5) (2022).

27. A. Nikolskaya, E. Okulich, D. Korolev, A. Stepanov, D. Nikolichev, A. Mikhaylov, D. Tetelbaum, A. Almaev, C. A. Bolzan, A. Buaczik, R. Giulian, P. L. Grande, A. Kumar, M. Kumar and D. Gogova, *Journal of Vacuum Science & Technology A* **39** (3) (2021).

28. K. Sasaki, M. Higashiwaki, A. Kuramata, T. Masui and S. Yamakoshi, *Applied Physics Express* **6** (8) (2013).

29. L.-Q. Zhang, W.-Q. Miao, X.-L. Wu, J.-Y. Ding, S.-Y. Qin, J.-J. Liu, Y.-T. Tian, Z.-Y. Wu, Y. Zhang, Q. Xing and P.-F. Wang, *Inorganics* **11** (10) (2023).

30. M. H. Lee, T. S. Chou, S. Bin Anooz, Z. Galazka, A. Popp and R. L. Peterson, *ACS Nano* **16** (8), 11988-11997 (2022).

31. A. Karim, Y. Song, D. C. Shoemaker, D.-W. Jeon, J.-H. Park, J. K. Mun, H. K. Lee and S. Choi, *Applied Physics Letters* **123** (19) (2023).

32. T. Zhao, X. Yu, W. Xu, Y. He, Z. Qu, R. Shen, R. Wang, H. Guo, H. Sun, Z. Li, M. Zhou, T. You and X. Ou, in *2024 IEEE International Electron Devices Meeting (IEDM)* (2024), pp. 1-4.

33. S. Mu and C. G. Van de Walle, *Physical Review Materials* **6** (10) (2022).

34. S. D. Lee, K. Akaiwa and S. Fujita, *physica status solidi c* **10** (11), 1592-1595 (2013).

35. S.-D. Lee, Y. Ito, K. Kaneko and S. Fujita, *Japanese Journal of Applied Physics* **54** (3) (2015).

36. J. Moloney, O. Tesh, M. Singh, J. W. Roberts, J. C. Jarman, L. C. Lee, T. N. Huq, J. Brister, S. Karboyan, M. Kuball, P. R. Chalker, R. A. Oliver and F. C. P. Massabuau, *Journal of Physics D: Applied Physics* **52** (47) (2019).

37. R. Jinno, K. Kaneko and S. Fujita, *AIP Advances* **10** (11) (2020).

38. J. P. McCandless, C. S. Chang, K. Nomoto, J. Casamento, V. Protasenko, P. Vogt, D. Rowe, K. Gann, S. T. Ho, W. Li, R. Jinno, Y. Cho, A. J. Green, K. D. Chabak, D. G. Schlom, M. O. Thompson, D. A. Muller, H. G. Xing and D. Jena, *Applied Physics Letters* **119** (6) (2021).

39. J. Tang, K. Jiang, P.-S. Tseng, R. C. Kurchin, L. M. Porter and R. F. Davis, *Applied Physics Letters* **125** (9) (2024).

40. Y. Choi, C. Kim, Y. Hwang, S. Park, H. Y. Kang, S. Chakraborty and R. B. K. Chung, *Crystal Growth & Design* **25** (4), 1023-1029 (2025).

41. G. T. Dang, T. Yasuoka, Y. Tagashira, T. Tadokoro, W. Theiss and T. Kawaharamura, *Applied Physics Letters* **113** (6) (2018).

42. X. Sun, W. Wei, F. F. Ren, X. Cui, S. Gu, R. Zhang, Y. Zheng and J. Ye, *J Chem Phys* **163** (9) (2025).

43. T. Uchida, K. Kaneko and S. Fujita, *MRS Advances* **3** (3), 171-177 (2018).

44. G. T. Dang, Y. Tagashira, T. Yasuoka, L. Liu and T. Kawaharamura, *AIP Advances* **10** (11) (2020).

45. B. Cullity, *Elements of X-ray Diffraction*. (Hsin Yueh, 1986).

46. Y. Cai, C. Zhu, L. Jiu, Y. Gong, X. Yu, J. Bai, V. Esenadag and T. Wang, *Materials* **11** (10), 1968 (2018).